chemosensors

MDPI

Article

Visible-Light-Driven Room Temperature NO_2 Gas Sensor Based on Localized Surface Plasmon Resonance: The Case of Gold Nanoparticle Decorated Zinc Oxide Nanorods (ZnO NRs)

Qomaruddin [1,2,3,*], Olga Casals [1], Hutomo Suryo Wasisto [2], Andreas Waag [2], Joan Daniel Prades [1] and Cristian Fàbrega [1,*]

[1] MIND-IN2UB, Department of Electronics and Biomedical Engineering, University of Barcelona, 08028 Barcelona, Spain; olga.casals@ub.edu (O.C.); dprades@ub.edu (J.D.P.)
[2] Institute of Semiconductor Technology (IHT) and Laboratory for Emerging Nanometrology (LENA), Technische Universität Braunschweig, 38106 Braunschweig, Germany; h.wasisto@tu-braunschweig.de (H.S.W.); a.waag@tu-braunschweig.de (A.W.)
[3] Research Center for Physics, National Research and Innovation Agency (BRIN), South Tangerang 15314, Indonesia
* Correspondence: qomaruddin@brin.go.id (Q.); cfabrega@ub.edu (C.F.); Tel.: +34-934-034-804 (Q. & C.F.)

Abstract: In this work, nitrogen dioxide (NO_2) gas sensors based on zinc oxide nanorods (ZnO NRs) decorated with gold nanoparticles (Au NPs) working under visible-light illumination with different wavelengths at room temperature are presented. The contribution of localized surface plasmon resonant (LSPR) by Au NPs attached to the ZnO NRs is demonstrated. According to our results, the presence of LSPR not only extends the functionality of ZnO NRs towards longer wavelengths (green light) but also increases the response at shorter wavelengths (blue light) by providing new inter-band gap energetic states. Finally, the sensing mechanism based on LSPR Au NPs is proposed.

Keywords: chemi-resistive sensor; gas sensors; gold nanoparticles; LSPR; photo-activated; room temperature; surface plasmon resonance; visible-light-driven; ZnO nanorods

Citation: Qomaruddin; Casals, O.; Wasisto, H.S.; Waag, A.; Prades, J.D.; Fàbrega, C. Visible-Light-Driven Room Temperature NO_2 Gas Sensor Based on Localized Surface Plasmon Resonance: The Case of Gold Nanoparticle Decorated Zinc Oxide Nanorods (ZnO NRs). *Chemosensors* **2022**, *10*, 28. https://doi.org/10.3390/chemosensors10010028

Academic Editor: Gabriella Leo

Received: 27 November 2021
Accepted: 4 January 2022
Published: 11 January 2022

1. Introduction

Gas pollutants have become, in recent years, one of the main concerns of people living in densely populated areas. The increasing awareness of their inhabitants about the potential adverse health effects of hazardous gases has encouraged administrations to establish new regulations about air quality in indoor and outdoor spaces. Among them, nitrogen dioxide (NO_2) is a pollutant gas produced in many of the combustion processes related to heating, industry, and transportation [1]. Traditionally, metal oxide semiconductor (MOX)-based chemi-resistive gas sensors are superior to other signal transduction solutions that are usually based on measuring optical or capacitive properties. This is due to the simplicity of setting up the resistance measurement circuit. The operation of resistive gas sensors is usually based on changes in resistivity or conductivity in semiconductor materials, which are due to a series of chemical steps on the surface, including the adsorption, reaction, and desorption of gas molecules [2]. Many efforts have been invested to make such sensors more sensitive, selective, stable, durable, energy efficient, and safe.

In a typical chemi-resistive configuration, the semiconducting sensor head is required to be heated to an elevated temperature in order to activate the reaction mechanisms involved in the detection process. However, the main drawback of chemi-resistive gas sensors to be introduced in the market as a mass product is their high power requirements [3–5]. To overcome these limitations, researchers have shifted their focus towards either reducing the working temperature of the sensing materials [6–9] and/or limiting the power consumption [10–15]. Several strategies have been proposed to solve these issues, such as modifying the band gap of the sensing materials [16,17], decorated metal nanoparticles [2,6,18–23],

and photo-activated materials [2,8,13,16,19,21,24–32]. Among them, photo-activated materials are one of the best options to circumvent the necessity of using temperature to activate the reaction mechanisms. Generally, photo-activated gas sensors rely on UV-light activation [29,31,32] since most gas sensors are based on wide band gap metal oxides (e.g., SnO_2 and ZnO). Following this trend, researchers have been focused on reducing the energy needed to activate the reaction mechanisms (i.e., using visible light [6,16,28,29,33]): band gap engineering by choosing sensing materials with suitable bandgap, and localized surface plasmon resonance (LSPR) in metal nanoparticles [6,19–21,25,28,34].

In particular, the introduction of metal nanoparticles into the matrix of a MOX to induce the absorption of light due to the resonance effect on the nanoparticles stands out as one of the most promising approaches because of our ability to tune the absorption band by modifying the surface and shape of the nanoparticles [35]. Moreover, the role of these nanoparticles in the performance of the gas sensors is not limited solely to the absorption of light, but also includes other effects related to the interaction between the metal nanoparticles and the MOX that influence and modify the gas sensor characteristics [36].

In this paper, we present a NO_2 gas sensor based on ZnO nanorods (NRs) decorated with gold nanoparticles (Au NPs) able to work at room temperature. The LSPR properties of Au NPs enhanced the absorption in the visible range (around 600 nm) providing sufficient energy to promote the reaction mechanisms and improving the sensor response compared to the bare ZnO NRs. Even though a similar work has been conducted by Chunxu Chen, et al. [37], our work offers a more in depth description of the mechanisms governing the gas sensor reactions and their performance. Furthermore, a detailed description of the influence of the Au NPs on the characteristics of our sensor is provided. In addition, we also show that the presence of Au NPs not only extends the absorption to the visible band but also improves the response and recovery of gas sensors.

2. Materials and Methods

2.1. Materials and Sensor Preparation

Gold-interdigitated electrodes (Au-IDE) on glass (MicruX Technology, Asturias, Spain) were used as an electronic platform to measure the electrical characteristics of the ZnO NRs. The IDE size was (10 × 6 × 0.75) mm, with 90 pairs of electrodes separated by 10 µm and 10 µm width. ZnO NRs were synthesized by hydrothermal method as follows: a zinc acetate dehydrate ($Zn(OOCH_3)_2{\cdot}2H_2O$, Sigma Aldrich) (25 mM) without additional purification dissolved in 10 mL of ethylene glycol was used as a seed layer. The seed layer was deposited onto IDE by a spin coating process. A total of 5 µL of the seed layer solution was drop casted onto the IDE followed by a spin coating process (500 rpm for 10 s and 5500 rpm for 20 s). In order to evaporate the solvent, the samples were heated on a hotplate at 90 °C for a few minutes. This process was repeated 3 times to ensure full coverage of the IDEs. Afterwards, an annealing process at 320 °C for 20 min (5 °C/min) was applied to fix the seed on the IDE and remove all the organic compounds. Zinc oxide nanorods (ZnO NRs) were grown by a hydrothermal method: 30 mM of Zn acetate dehydrate ($Zn(OOCH_3)_2{\cdot}2H_2O$) and 30 mM of hexamethylenetetramine (HTM) ($C_6H_{12}N_4$) was dissolved in 25 mL of Millipore water as a growth solution. The sample was immersed in the growth solution for 3–5 h at 90 °C. Then, thermal treatment at 350 °C in the air for 1 h was applied to remove the residual organic compounds and crystallize the sample. This procedure is shown in Figure 1a.

Gold colloidal (20 nm, concentration: ~0.01% $HAuCl_4$, ~1 A_{520} units/mL) were purchased from Sigma-Aldrich and used without any additional treatment. An electrophoresis method was applied to attach the Au NPs onto the surface of the ZnO NRs. A previously fabricated ZnO NR sample (ZnO NRs on IDE) was immersed in the Au NP gold suspension for 300 s, in which a constant voltage (3V) between the IDE and electrode was simultaneously applied. The ZnO NRs that covered half of the IDE is shown in Figure 1b to simplify the view of IDE, ZnO NRs and the expected result of the Au NP decoration.

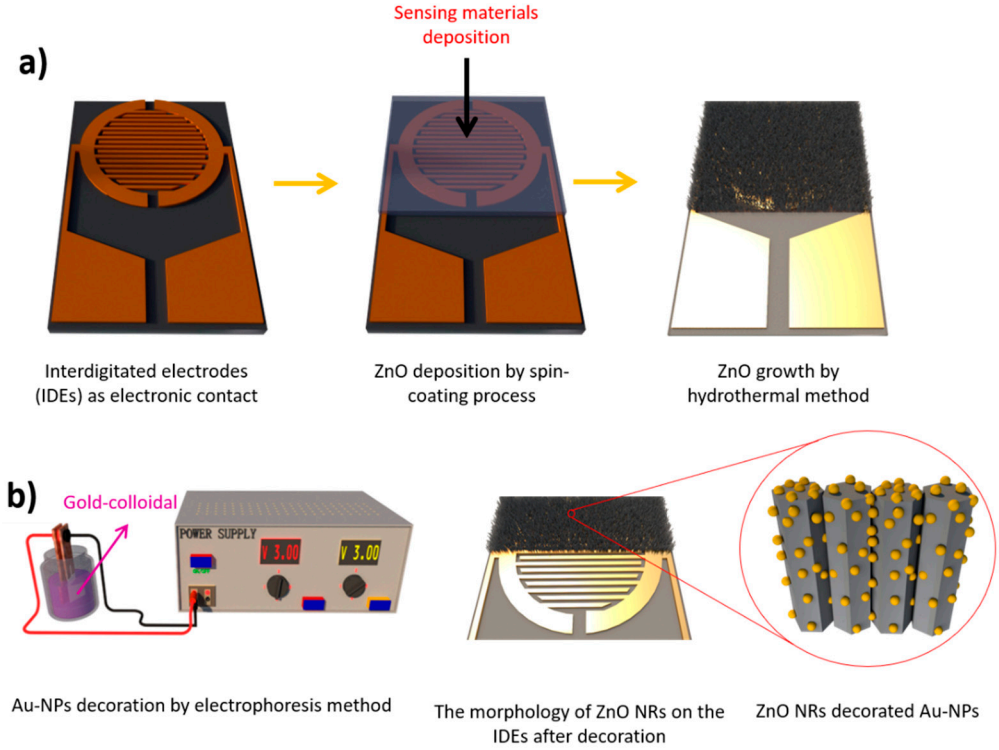

Figure 1. (**a**) Seed layer deposition on IDE by a spin-coating process followed by the growth process by hydrothermal method and (**b**) Au NP decoration by the electrophoresis technique.

2.2. Materials Characterization

The morphology and elemental composition of as-grown bare ZnO NRs and decorated Au NPs were studied using JSM-7100F thermal field emission scanning electron microscope (FE-SEM) and energy dispersive spectroscopy (EDS). To know the 3D surface profile, an atomic force microscope (AFM) analysis was conducted by Veeco Dimension 3100. The optical properties were measured using Specord® PC 205 ultraviolet-visible (UV-vis) spectrophotometers, Analytik Jena AG, Jena, Germany and photoluminescence (PL) spectra at room temperature.

2.3. Gas Measurement

Figure 2 is a schematic of the measurement system for light-activated gas sensing response. The experiments of gas measurement were performed in a customized chamber of 200 mL in volume. The gas flow was maintained steady at 200 mL/min during all the experiments. The gas chamber was equipped with sealed feedthrough electrical connections to drive the light-emitting diodes (LEDs) and to measure the electrical resistance of the ZnO NRs, using a Keithley 2400 source measure unit (SMU). The LED driving and resistance measurements were carried out under constant current conditions. The desired atmospheric conditions were provided by independent mass flow controllers blending between synthetic air (SA), carbon monoxide (100 ppm of CO in SA), carbon dioxide (500 ppm of CO_2 in SA), and nitrogen dioxide (10 ppm of NO_2 in SA) at convenience. To investigate the optoelectronic properties of ZnO NRs and ZnO NRs/Au NPs, conductance measurements were performed under synthetic airflow with different LED wavelengths of visible light irradiation (i.e., blue (465 nm), green (520 nm), yellow (590 nm) and red (640 nm)) and in dark conditions. In this regard, during the experiment, the intensity of LEDs applied was 10 mW/cm^2. In that regard, our group has recently developed a micro light platform where an LED is embedded beneath an IDE with power consumptions in the microwatt (μW) range (i.e., 30 μW to detect 250 ppb of NO_2 with ZnO NPs) [13]. In order to determine the sensitivity of the ZnO NR sensors towards particular gases, different concentrations of NO_2 from the low to the high concentrations (i.e., 0.5, 1, 2, 3, 5, and 10 ppm) were then exposed

to the chamber under LED irradiation. The response (sensitivity) of NO_2 was calculated from the relation as follows:

$$S(\%) = \frac{(R_{NO_2} - R_{air})}{R_{air}} \times 100\% \quad (1)$$

where R_{NO_2} and R_{air} are the electrical resistance of the sensor when exposed to NO_2 gas and in air, respectively. The definition of the response time and recovery time is the time needed to reach 90% of the total resistance change during the chemisorption (adsorption and desorption) process. Furthermore, all experiments were conducted at room temperature.

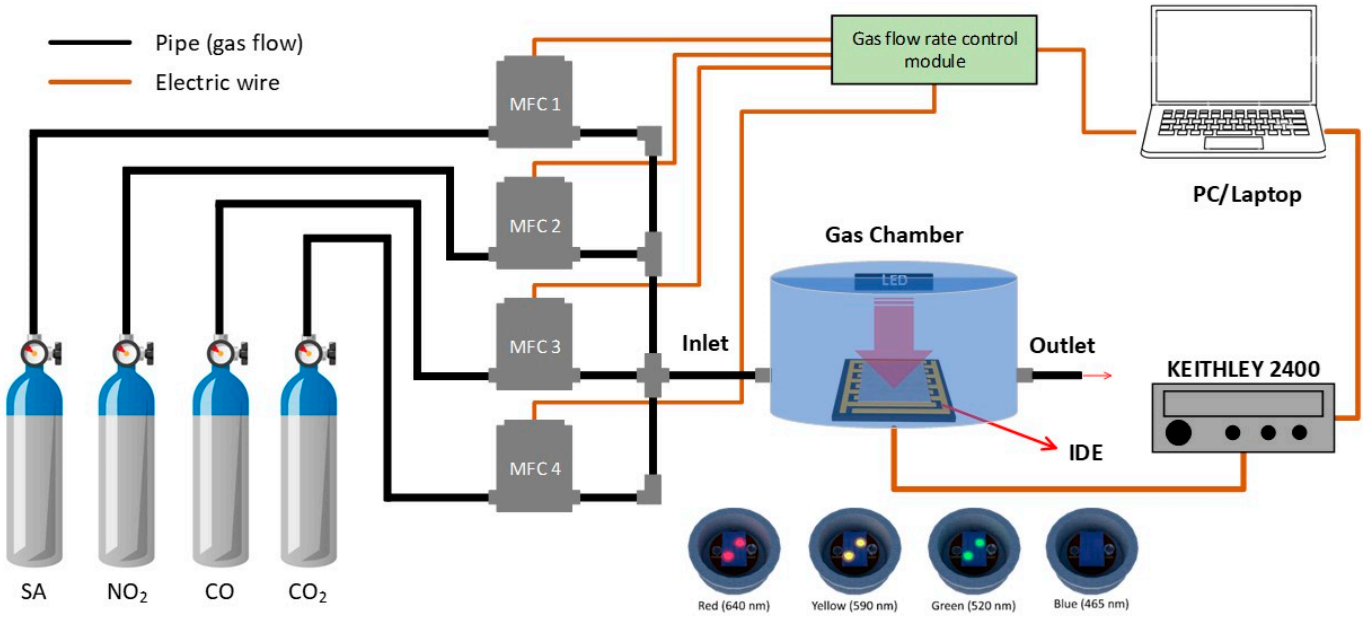

Figure 2. Schematic of the measurement system for light-activated gas sensing response.

3. Results

3.1. Active Material Characteristic

Energy dispersive X-ray spectroscopy (EDS) was applied to measure the chemical composition of the produced active materials. A typical EDS spectrum in Figure 3a confirms the existence of zinc and oxygen, revealing the successful formation of ZnO. In addition, the successful formation of ZnO decorated Au NPs is confirmed by the other peak of gold, which is observed in Figure 3b.

Figure 4a,b shows the field emission scanning electron microscopy (FE-SEM) image of bare ZnO NRs and ZnO NRs/Au NPs with different magnifications. ZnO NRs presented a hexagonal shape due to the preferential growth along the <0001> direction [38] of the wurtzite crystal structure (JCPDS 01-075-0576). All samples displayed a uniform NRs distribution and density throughout the sample with diameters ranging from 150–180 nm. After the electrophoresis process, Au NPs were uniformly and completely attached to the surface of the ZnO NRs. The length of the NRs was measured by atomic force microscopy (AFM). A region with faulty growth was used to measure a profile line resulting in a height of around 1 μm (Figure 4d).

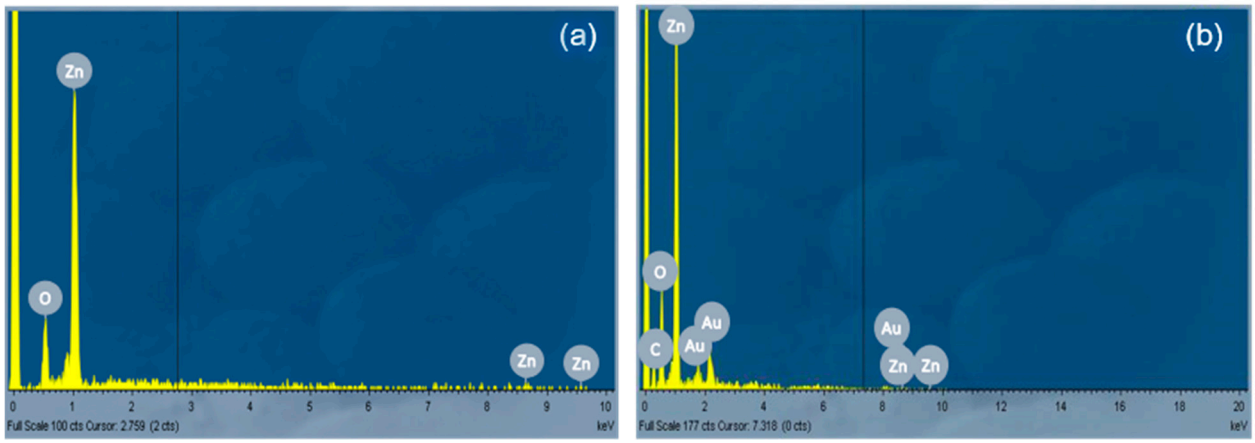

Figure 3. (**a**) Energy dispersive X-ray spectroscopy (EDS) patterns of bare ZnO NRs and (**b**) ZnO NRs/Au NPs, confirming the existence of Zn, O, and Au, and revealing the successful formation of ZnO NRs and Au NPs decoration.

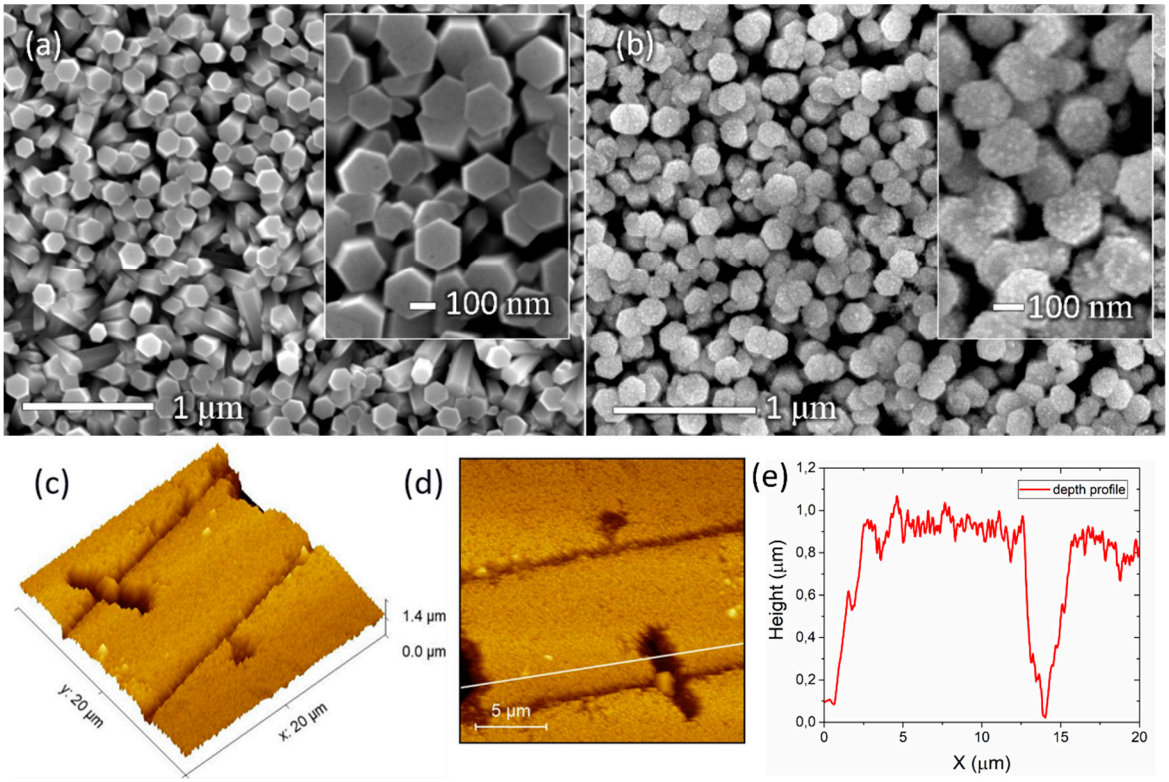

Figure 4. Field emission scanning electron microscopy (FE-SEM) images of (**a**) bare ZnO NRs and (**b**) ZnO NRs/Au NPs with different magnifications. (**c**,**d**) A 3D AFM image for ZnO NRs and (**e**) depth profile of ~1 µm due to the limitation of tip size of AFM.

Figure 5a shows the UV-vis diffuse reflectance spectra (UV-vis DRS) of ZnO NRs and ZnO NRs/Au NPs where the contribution of Au NPs is clearly evidenced by an absorption band of around 550 nm corresponding to the LSPR gold band [19,25]. According to the result, the absorption spectrum broadened to the visible light range around 500–600 nm. In this particular case, there is a chance to generate the energy of resonance when the frequency of the photon of incident light fits the coherent oscillation frequency of conduction electrons confined at the Au NPs surface [6].

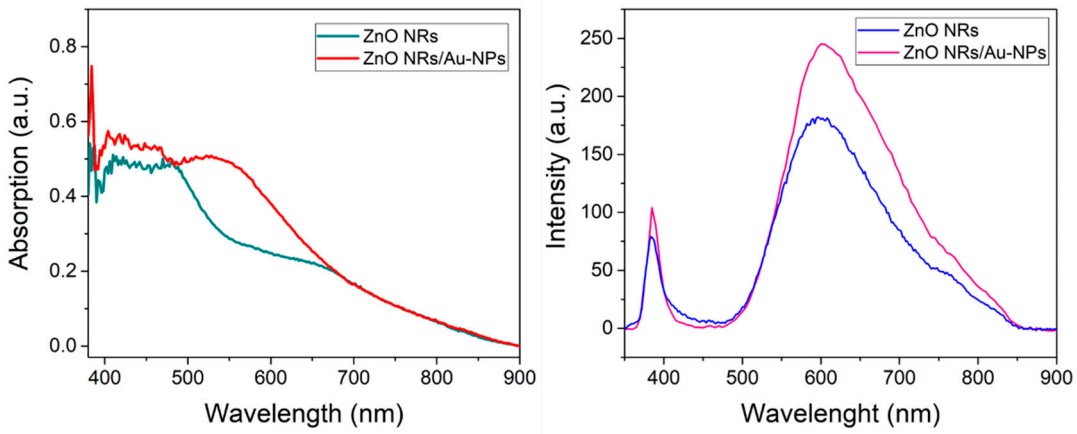

Figure 5. (**a**) Optical absorption ultraviolet-visible light diffuse reflectance spectra (UV-vis DRS) confirming the enhancement of absorption spectra in the range of 500–600 nm. (**b**) Photoluminescence (PL) spectra of the bare ZnO NRs and ZnO NRs/Au NPs at deep level (DL) emission spectra.

Figure 5b illustrates the photoluminescence (PL) spectra of bare ZnO NRs and ZnO NRs/Au NPs, revealing two peaks where the UV line relates to the near band gap emission (NBE) and is assigned to the radiative recombination of excitons, whereas the deep level (DL) emission is attributed to the charge carrier relaxation via surface-related trap states in the visible range [24,39]. The sensors of ZnO NRs/Au NPs show an increment in emission compared to that of bare ZnO NRs, which is likely due to the enhanced light trapping within the structures. The DL emission from ZnO NRs/Au NPs is significantly higher than the bare ZnO NRs. According to the result, this effect might be due to new deep-level traps states because of the presence of the Au NPs. However, other groups [25,35] found a completely opposite trend when decorating ZnO NRs with gold nanoparticles, i.e., the emission band associated with the trap states are quenched compared to the bare ZnO NRs because these photons are absorbed by the Au NPs throughout the surface plasmon resonance whose absorption wavelength is typically around 550–600 nm. The intensity and the ratio of the NBE to DL emission vary obviously with the different deposition times of Au NPs [34]. Furthermore, these ZnO NRs were decorated with Au NPs for 300 s. The enhancement of the SPR achievement is affected by the light emission and surface plasmon resonance of the Au NPs energy. Moreover, the shapes and sizes of nanoparticles closely affect the frequency of the SPR. [35].

3.2. Sensor Measurement

In order to know the response of the sensor to photo-activation, an ON/OFF mode was then conducted without gas under LED illumination with different wavelengths. Figure 6a,b shows the responses for the bare ZnO NRs and ZnO NRs/Au NPs under LED illumination with different wavelengths. The contribution of the LSPR absorption band is evidenced by the photoexcitation under 590 and 640 nm LED illumination.

To investigate the sensitivity of the ZnO NRs sensors towards oxidizing gases (i.e., NO_2), different concentrations of nitrogen dioxide (i.e., 0.5, 1, 2, 3, 5, and 10 ppm) were then applied to the chamber under LED illumination with different wavelengths. Before introducing the target gases, a 2 h stabilization step with SA in the chamber was conducted to achieve a reference baseline. Then, 10 ppm of NO_2 was introduced to the chamber for 30 min and then removed by introducing again SA until the next NO_2 level concentration. The same procedure was conducted for different wavelengths of LED illumination during the experiment. Figure 7, by referring to Figure 6b, shows the dynamic responses of ZnO NRs/Au NPs to different concentrations of NO_2 under blue, green, yellow, and red LED illumination. As expected, exposing ZnO (*n*-type) to an oxidizing gas (NO_2) leads to an increase in the resistance of the MOX with a response proportional to the gas concentration. Upon light illumination and depending on its energy, the sensor behavior is completely

different. For example, in dark conditions, the resistance of the sample begins to rise once the NO_2 interacts with the surface of the ZnO NRs. After ceasing the exposure to NO_2, the resistance does not recover to its original value, meaning that there is not enough energy to release the adsorbed NO_2 onto the surface of ZnO NRs (remember, samples are at room temperature). This behavior is reproduced with red and yellow illumination, where the energy of the photons is not sufficient to promote the desorption of the NO_2. Only when green and blue light are used, the characteristic adsorption/desorption process can be observed, including the saturation regime after enough time. Since the adsorption/desorption process emerged for the blue and green LED, we calculated the sensitivity, response time, and recovery time for them. Figure 8 shows more detailed response differences between bare the ZnO NRs and ZnO NRs/Au-NPs. The sensitivity value of the sensors using blue and green LED are 891% and 191% at 10 ppm of NO_2, respectively, while their response time for the blue and green LED is 18 min and 21 min, respectively.

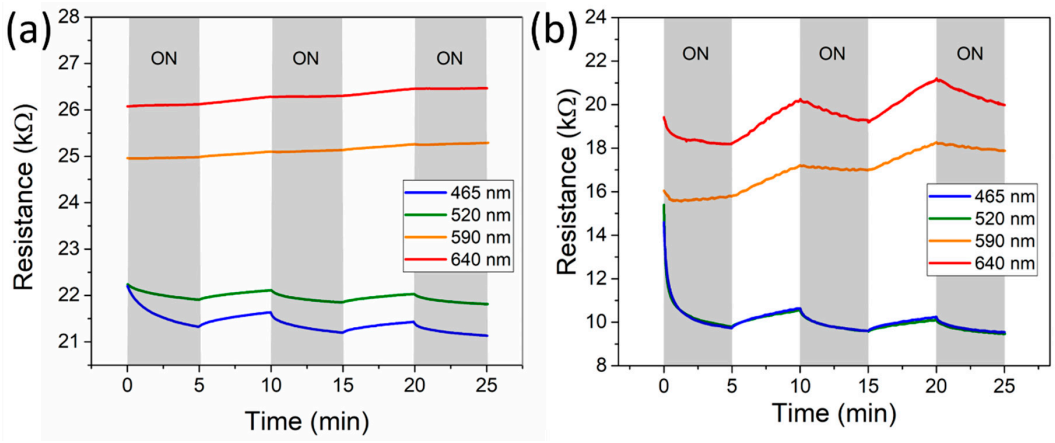

Figure 6. Visible-light-activated on ZnO NRs (ON/OFF mode) for (**a**) the bare ZnO NRs and (**b**) decorated Au NPs.

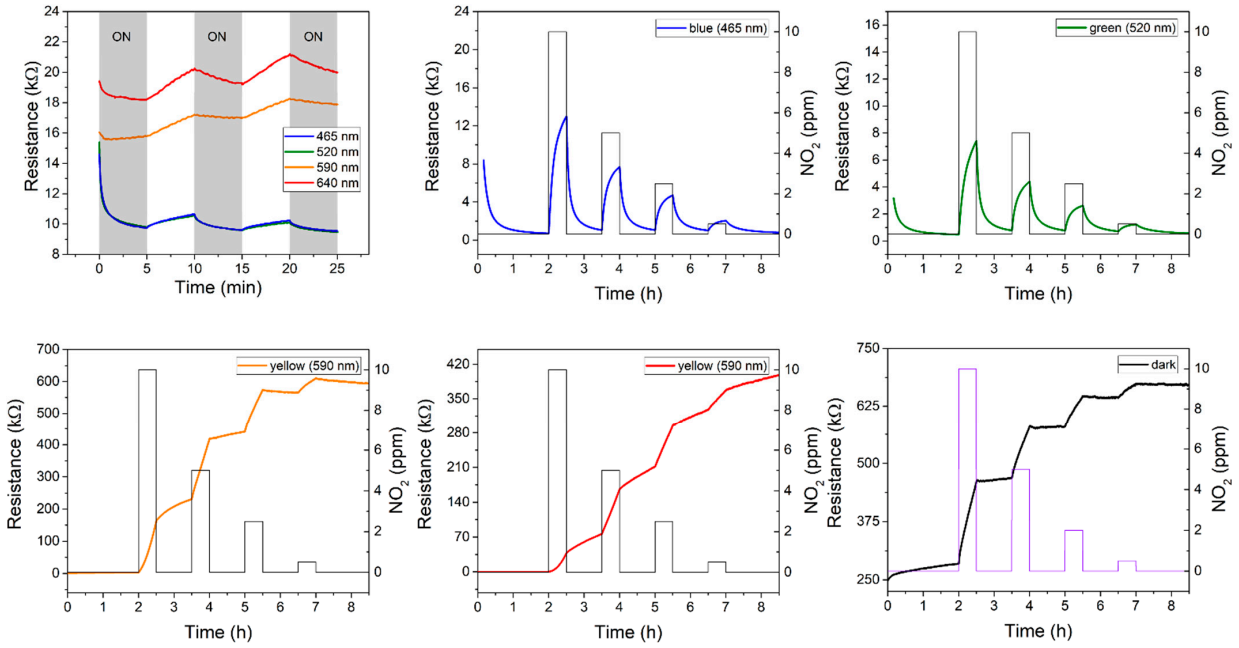

Figure 7. The dynamic sensing responses of ZnO NRs/Au NPs. The adsorption/desorption process emerged on blue and green LED due to their energy. Meanwhile, for the yellow, red LED, and dark conditions, the energy is not sufficient to release the adsorbed NO_2 onto the surface of ZnO NRs at room temperature.

To appreciate the role of the Au NPs on the performance of the gas sensor, a detailed performance comparison between the bare ZnO NRs and the ZnO NRs/Au NPs were conducted at different wavelengths (Figure 8). In both cases, we have the same trend described previously. However, the presence of Au NPs has, at least, three different contributions to the performance of the gas sensor: (1) to foster the adsorption of NO_2 onto the surface, both in dark and under light conditions; (2) to increase the response towards NO_2 under green and blue illuminations; and (3) to improve the desorption rate of NO_2 under green and blue illumination. Therefore, the contribution of the Au nanoparticles extends beyond the introduction of a new absorption band (around 600 nm).

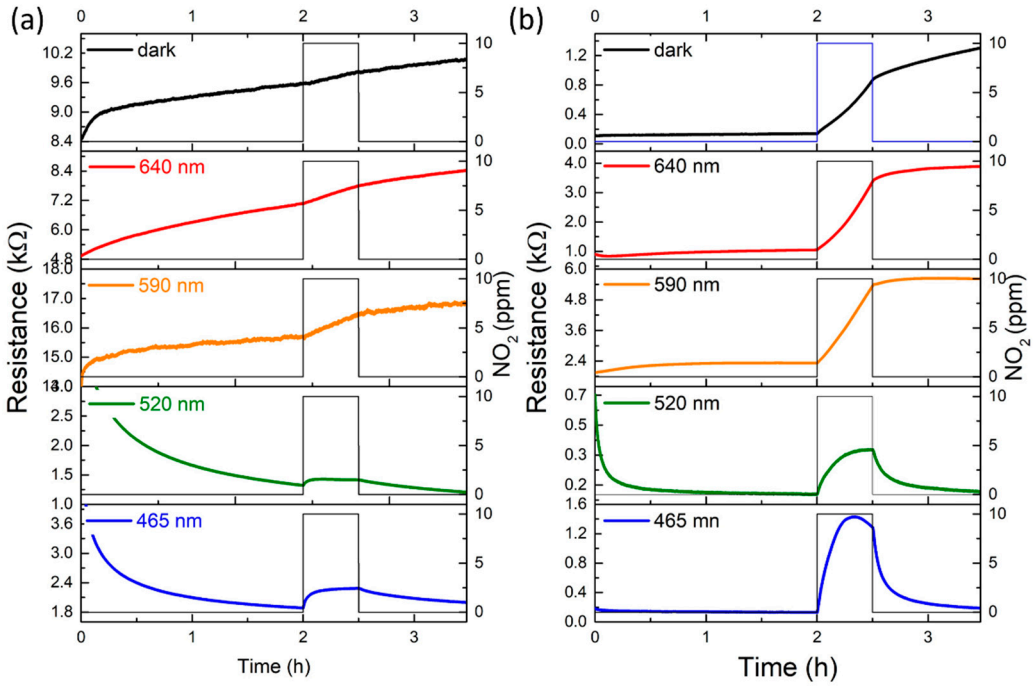

Figure 8. Sensing responses of (**a**) the bare ZnO NRs and (**b**) the ZnO NRs/Au NPs. The sensitivity for green and blue LED of the bare ZnO NRs is 7.2% and 19.3%, respectively, while the ZnO NRs/Au NPs is 191% and 891%, respectively, for the green and blue LED.

Cross-sensitivity experiments towards CO and CO_2, which are common gases in the ambient air, were conducted with the aim of determining the sensing selectivity of ZnO NR/Au NPs. A typical experiment consisted of introducing, first, a certain amount of NO_2 (10 ppm) followed by a certain concentration of either CO (100 ppm) or CO_2 (500 ppm), and finally a mixture of both gases with the same previous concentrations. Figure 9a,b depicts the transient experiment of such experiment for CO (a) and CO_2 (b). When the interfering gas is introduced into the chamber alone, the response of the sensor is practically null in the case of CO. However, when introducing CO_2, a decrease in the resistance of the sensor is clearly appreciable even though the baseline is partially shadowing this effect. The observed reduction of the resistance is consistent with the fact that CO_2 is a reducing gas. Finally, when both gases, NO_2 and the interfering one, were blended into the chamber, no cross-interferences were evident in the case of CO, but a clear dampening of the response can be observed in the case of CO_2. This cross-interfering phenomenon is the result of the competition between an oxidizing gas (NO_2), which leads to an increase in resistance, and a reducing gas (CO_2) with the opposite effect, a decrease in the resistance.

Moreover, another parameter that can influence the sensor performance, in photo-activated and low-power consumption applications, is the intensity of the LED illumination. Figure 9c shows the responses of the ZnO NRs/Au NPs sensor with different intensities of blue LED. By applying three different intensities (i.e., 1, 5, and 10 mW/cm^2) to 10 ppm of NO_2, the response of the sensor was obviously different. Even though we cannot conclude

that a lower intensity has a higher sensitivity, since there is no baseline of the resistance for each intensity, we can assure that the intensity of the LED had a clear effect on the shape of the response signal. Note that the higher the intensity, the faster the saturation regime is reached where the absorption and desorption processes achieve an equilibrium. Therefore, this kind of experiment is very important to estimate the minimum energy or power needed with the aim of minimizing power consumption.

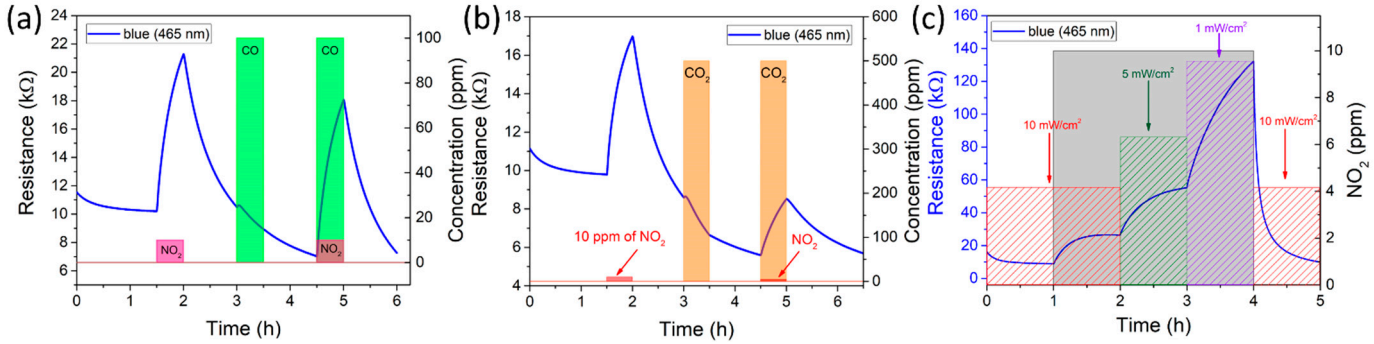

Figure 9. The response of cross-sensitivity by introducing a high concentration of interfering gas, (**a**) 100 ppm of CO and (**b**) 500 ppm of CO_2, in order to investigate the selectivity of the sensors. (**c**) The response of the sensors with different intensities of the blue LED (i.e., 1, 5, and 10 mW/cm^2) to 10 ppm of NO_2.

The comparison of the sensor response in this work and the previously published reports is shown in Table 1. The contribution of Au NPs decoration on ZnO-based gas sensors indicates a high performance under particular conditions, especially under visible-light-driven conditions at room temperature. The increased absorption after Au NPs decoration leads to the generation of the energetic charge on the surface of the sensors that enhances the sensitivity of the sensors.

Table 1. The performance comparison ZnO-based gas sensors decorated Au NPs with different operating conditions.

Materials	Target Gas	Operating Condition *	Sensitivity (%)	Ref
Au/ZnO thin film	NO_2—10 ppm	RT, λ_{blue} = 439 nm, 0.76 mW/cm^2	~10.00	[2]
ZnO/Au NPs	NO_x—6 ppm	RT, white light (~400 μW/cm^2)	130.00	[8]
ZnO-rGO-Au	NO_2—100 ppm	80 °C	32.55	[40]
Au/ZnO NRs	CO—1000 ppm	150 °C	12.00	[41]
	NO_2—50 ppm	300 °C	4.14	
ZnO:Au NPs	Ethanol—1000 ppm	RT, UV = 254 nm, 4.1 mW/cm^2	1.46	[42]
		125 °C, UV = 254 nm, 4.1 mW/cm^2	6.30	
Au-ZnO NRs array films	NO_2—1–5 ppm	RT, λ = 495 nm, 50 mW/cm^2	1.25	[37]
ZnO NRs/Au NPs	NO_2—10 ppm	RT, vis-light (465–640 nm), 10 mW/cm^2	891.00	This work

* Particular condition means the working temperature, wavelength (λ) and the intensity of the light (LED).

4. Discussion

Light-Activated and Sensing Mechanism

According to the UV-vis and PL spectra, the defect emission of ZnO NRs was attributed to the electron transition from a deep-level trap to the valence band of ZnO [3,5,18]. Due to LSPR, the absorption spectrum of Au NPs overlaps with the defect-related emission bands of ZnO NRs in the visible range, and it is impossible to directly couple with the NBE of ZnO NRs. In other words, resonant energy coupling must occur between the defect emission of ZnO NRs and LSPR. In addition, Au NPs can absorb the visible light photon energy emitted by ZnO NRs, which excites the electrons of the Au NPs to a higher energy state and then transfers them to DL emission through the CB of ZnO NRs. The energy transfer is in control of the change of defect energy level emission. With the support of the

resonance energy coupling process, electrons with higher energy can be well transferred to the conduction band of ZnO NRs, resulting in enhanced NBE and DL emissions of ZnO NRs, as shown in the schematic diagram in Figure 10. Particularly, the energy emitted by photonic ZnO NRs DL can be resonantly absorbed by Au NPs to generate LSPR, which excites the electrons of Au NPs to a higher energy state and then transfers them to the conduction band of ZnO NRs. According to the schematic diagram, the enhancement of the emission intensity of NBE and DL is related to the following factors: (1) the coupling efficiency indicated by the degree of overlap between the emission spectrum of ZnO NRs defect and the absorption spectrum of Au NPs; (2) the coupling intensity indicates the absorption of Au NPs; and (3) the local field caused by the hot-spots effect the enhancement is affected by the morphology and spatial density of Au NPs on the surface of ZnO NRs [34].

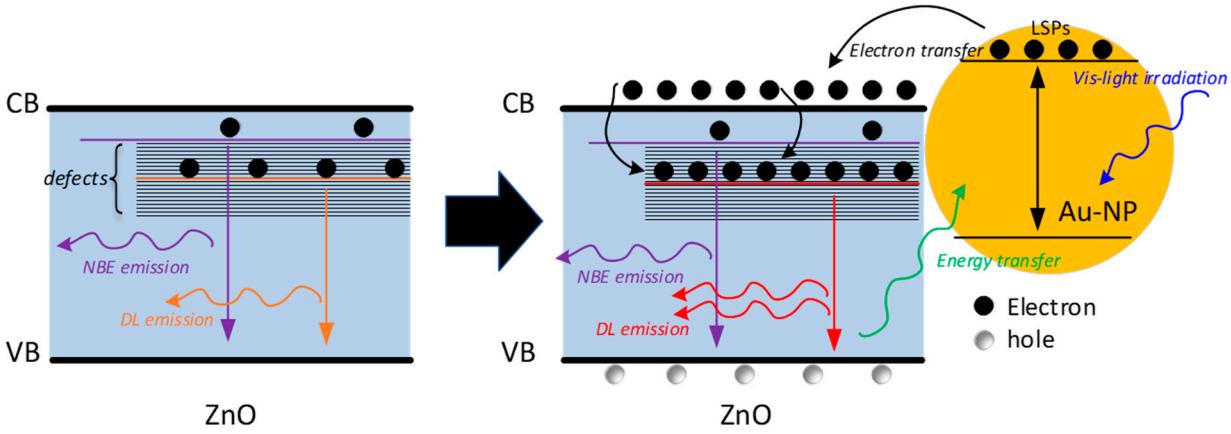

Figure 10. Schematic of electron transfer in energy band diagram of ZnO NRs/Au NPs with localized surface plasmon of Au NPs according to the PL spectra.

Generally, the working principle of metal oxide-based gas sensors depends on the chemically adsorbed (adsorption and desorption) oxygen molecules on the surface, which are ionized into substances, such as O_2^-, O^- and O^{2-}, by capturing electrons near the surfaces of the metal oxides. Moreover, it is known that O_2^-, O^- and O^{2-} ionsorption species dominate at <150 °C, between 150 and 400 °C, and at >400 °C, respectively [43]. When ZnO NRs are exposed to the air at room temperature in dark conditions, some oxygen molecules are absorbed by the surface and then trap free electrons from the conduction band of ZnO NRs $(O_{2\ (g)} + e^- \leftrightarrow O^-_{2(ads)})$ [26]. Correspondingly, the electron carrier density in ZnO NRs decreases, forming an electron depletion layer to compensate for the negative charge of surface oxygen species (see Figure 11a) [44]. When the ZnO NRs are exposed to vis-light, electron-hole pairs will be generated, and then the holes can migrate to the surface of ZnO NRs and be neutralized by pre-chemisorb oxygen ion $(h^+ + O^-_{2\ (ads)} \leftrightarrow O_{2(g)})$ [29]. At the same time, photo-generated electrons can combine with oxygen molecules in the air to form additional photo-generated oxygen ions, as in the following equation (see Figure 11b):

$$(O_{2(g)} + e^-(h\nu) \leftrightarrow O^-_{2(ads)}(h\nu)) \quad (2)$$

Consequently, the electrical resistance of ZnO NRs decreases in this reaction. The adsorption and desorption of oxygen molecules on the surface of ZnO NRs can gradually reach a stable equilibrium state, and the carrier density of ZnO NRs under vis-light illumination is still much higher than that in dark [45]. A similar reaction also occurs in ZnO NRs/Au NPs since there is a contribution of electron transfer from Au NPs due to LSPR (Figure 11d). Therefore, a large photocurrent was observed under the vis-light irradiation with the energetic electron (hot electron) and more density of charge (Figure 11e). The increment of energetic charge on the surface leads to more sensitivity of the sensors. In the opposite case, the density of free electrons reduces quickly after illumination of the

vis-light is turned off, which leads to a decrease in the photocurrent and an increase in the electrical resistance (see Figure 6). All the chemisorption processes affect the width change of the EDL.

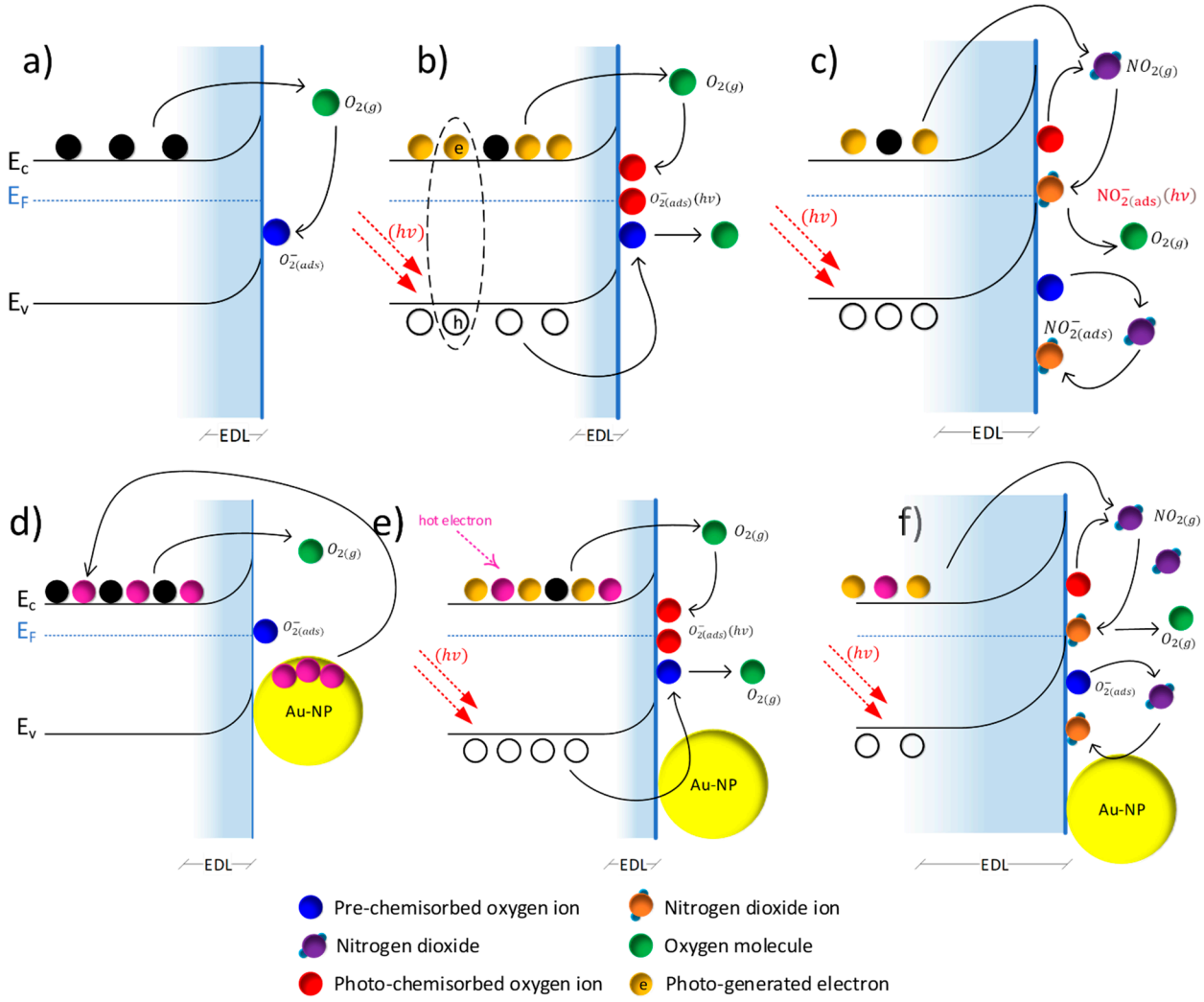

Figure 11. Schematic of electron transfer in energy band diagram of ZnO NRs when detecting NO_2 showing the effect of Au NP decoration. (**a**–**c**) The mechanism for bare ZnO NRs: (**a**) pre-chemisorbed oxygen ions are formed at RT in dark conditions, (**b**) under visible light illumination, and (**c**) during exposure to NO_2 molecules. (**d**–**f**) The mechanism for Au NP-decorated ZnO NRs: (**d**) More electrons are formed in conduction band by transferring them from Au NPs, (**e**) under visible light illumination, and (**f**) during exposure to NO_2 molecules.

Figure 11 shows a schematic of the proposed sensing mechanisms when the sensor is in dark conditions (before and after Au NPs decoration) and exposed to the target gas (NO_2) under visible-light irradiation together with the energy band diagram. When the chemisorbed oxygen molecules reach an equilibrium state, the new electron depletion layer is formed under the surface of Au NPs (Figure 11e). Once the sensors are exposed to NO_2 gas, as the electrons extracted from the conduction band or the remaining photo-generated electrons are transferred to the surface and increase the resistance of the sensor, a stronger chemical adsorption species $O^-_{2(ads)}(h\nu)$ is formed, and the depletion layer becomes thicker [7] as shown in Figure 11c,f. These reactions can be simply described as follows:

$$NO_{2(g)} + O^-_{2(ads)}(h\nu) \leftrightarrow NO^-_{2(ads)}(h\nu) + O_{2(g)} \quad (3)$$

$$NO_{2(g)} + e^{-}(h\nu) \leftrightarrow NO^{-}_{2(ads)}(h\nu) \quad (4)$$

$$NO_{2(g)} + O^{-}_{2(ads)} \leftrightarrow NO^{-}_{2(ads)} + O_{2(g)} \quad (5)$$

$$NO_{2(g)} + e^{-} \leftrightarrow NO^{-}_{2(ads)} \quad (6)$$

The species $NO^{-}_{2(ads)}(h\nu)$ is feebly bound to the surface and can be simply removed since the electron affinity of NO_2 (2.27 eV) is higher than that of O_2 (0.44 eV) [7]. When NO_2 gas is removed from the chamber, the photo-generated holes recombine with the electron captured by the chemisorbed $NO^{-}_{2(ads)}(h\nu)$ and $O^{-}_{2(ads)}(h\nu)$ recover the surface of nanoparticles via reaction (2), which returns the depletion layer to the initial state that corresponds to the decreased electrical resistance of the sensors. Therefore, under the actual experiment, the detection of NO_2 is controlled by the competition between oxygen molecules ($O_{2(g)}$), pre-chemisorbed oxygen ion ($O^{-}_{2(ads)}$), photo-absorbed oxygen ion ($O^{-}_{2(ads)}(h\nu)$) and nitrogen dioxide ($NO^{-}_{2(ads)}(h\nu)$) for the absorption process (reaction 2–6) and desorption process (reaction 7) as follows:

$$NO^{-}_{2(ads)}(h\nu) + h^{+} \leftrightarrow NO_{2(g)} \quad (7)$$

Thus, visible light acts as a regulator of the competition between these reaction pathways [1]. These mechanisms quantitatively predict the sensitivity of the sensors S(%) to different concentrations of nitrogen dioxide (NO_2) on the surface of ZnO NRs observed experimentally under different light intensities [27]. The oxygen molecules play an important role in the chemisorption (adsorption and desorption) process of NO_2 molecules on the ZnO NRs surface. The coverage degrees of $O^{-}_{2(ads)}(h\nu)$ directly influences performances (i.e., sensitivity, response, and recovery time) of photo-activated metal oxide gas sensors.

5. Conclusions

A visible-light-driven room temperature NO_2 gas sensor based on localized surface plasmon resonance (LSPR) was successfully fabricated by the electrophoretic deposition of gold nanoparticles (Au NPs) on zinc oxide nanorods (ZnO NRs) grown by a hydrothermal process. According to UV-vis and photoluminescence (PL) spectra, Au NPs decoration has a significant contribution to the improvement of the sensitivity of the sensor due to increasing energetic charge (hot electron) on the surface and LSPR phenomenon. The sensitivity of the sensor reached up to around 46 times of 891% for blue LED at 10 ppm of NO_2 after Au NPs decoration. Finally, a detailed description of the phenomenon governing the reaction mechanisms and the performance of the sensors were provided, proving that the role of the Au NPs extends beyond the mere extension of the light absorption to the visible region due to the LSPR phenomenon, by fostering the adsorption of NO_2, and improving the desorption rate and increasing the response of NO_2 under green and blue illumination conditions.

The results reported that LSPR could potentially lead to the development of good-performance chemi-resistive gas sensors operating at room temperature, which are energy-efficient, suitable, and safer to use in a hazardous environment. Moreover, one aspect that should be noted is that another factor that greatly influences the performance of the sensor in photo-activated, low power consumption, and RT working temperature regime, is light intensity. This will be an interesting challenge for sensor technology in the future.

Author Contributions: Data curation, Qomaruddin; Formal analysis, Qomaruddin and C.F.; Investigation, Qomaruddin and C.F.; Methodology, Qomaruddin; Resources, Qomaruddin and O.C.; Supervision, H.S.W., J.D.P. and C.F.; Writing—original draft, Qomaruddin; Writing—review & editing, Qomaruddin, O.C., H.S.W., A.W., J.D.P. and C.F. All authors have read and agreed to the published version of the manuscript.

Funding: The research leading to these results has received funding from the European Research Council under the European Union's Seventh Framework Program (FP/2007-2013)/ERC Grant Agreement n.336917.

Institutional Review Board Statement: Not applicable.

Informed Consent Statement: Not applicable.

Acknowledgments: Qomaruddin thanks to the Ministry of Research, Technology and Higher Education of the Republic of Indonesia (RISTEKDIKTI) for the PhD scholarship of RISET-Pro under ref. no. 348/RISET-Pro/ FGS/VIII/2016 and Indonesian-German Center for Nano and Quantum Technologies (IG-Nano) for the support. H.S.W. and A.W. acknowledge the project funding support within the LENA-OptoSense group from the Lower Saxony Ministry for Science and Culture (NMWK), Germany. This work has been carried out within the EU Project of "BetterSense–Nanodevice Engineering for Better Chemical Gas Sensing Technology" funded by the European Research Council under Grant Agreement No. 336917. J.D.P. acknowledges the support of the ICREA Academia Program and the DFG Project GRK NanoMet. Thanks are also owed to Nurhalis Majid and Winfried Daum (TU Clausthal, Germany) who provides the AFM measurement results.

Conflicts of Interest: The authors declare no conflict of interest.

References

1. Casals, O.; Markiewicz, N.; Fabrega, C.; Gràcia, I.; Cané, C.; Wasisto, H.S.; Waag, A.; Prades, J.D. A Parts Per Billion (Ppb) Sensor for NO_2 with Microwatt (MW) Power Requirements Based on Micro Light Plates. *ACS Sens.* **2019**, *4*, 822–826. [CrossRef] [PubMed]
2. Chinh, N.D.; Hien, T.T.; Do Van, L.; Hieu, N.M.; Quang, N.D.; Lee, S.-M.; Kim, C.; Kim, D. Adsorption/Desorption Kinetics of Nitric Oxide on Zinc Oxide Nano Film Sensor Enhanced by Light Irradiation and Gold-Nanoparticles Decoration. *Sens. Actuators B Chem.* **2019**, *281*, 262–272. [CrossRef]
3. Barsan, N.; Koziej, D.; Weimar, U. Metal Oxide-Based Gas Sensor Research: How To? *Sens. Actuators B Chem.* **2007**, *121*, 18–35. [CrossRef]
4. Park, S.; An, S.; Mun, Y.; Lee, C. UV-Enhanced NO_2 Gas Sensing Properties of SnO_2-Core/ZnO-Shell Nanowires at Room Temperature. *ACS Appl. Mater. Interfaces* **2013**, *5*, 4285–4292. [CrossRef]
5. Fabbri, B.; Gaiardo, A.; Giberti, A.; Guidi, V.; Malagù, C.; Martucci, A.; Sturaro, M.; Zonta, G.; Gherardi, S.; Bernardoni, P. Chemoresistive Properties of Photo-Activated Thin and Thick ZnO Films. *Sens. Actuators B Chem.* **2016**, *222*, 1251–1256. [CrossRef]
6. Zhang, Q.; Xie, G.; Xu, M.; Su, Y.; Tai, H.; Du, H.; Jiang, Y. Visible Light-Assisted Room Temperature Gas Sensing with ZnO-Ag Heterostructure Nanoparticles. *Sens. Actuators B Chem.* **2018**, *259*, 269–281. [CrossRef]
7. Zhang, C.; Geng, X.; Li, J.; Luo, Y.; Lu, P. Role of Oxygen Vacancy in Tuning of Optical, Electrical and NO_2 Sensing Properties of ZnO_{1-x} Coatings at Room Temperature. *Sens. Actuators B Chem.* **2017**, *248*, 886–893. [CrossRef]
8. Chakrabarty, P.; Banik, M.; Gogurla, N.; Santra, S.; Ray, S.K.; Mukherjee, R. Light Trapping-Mediated Room-Temperature Gas Sensing by Ordered ZnO Nano Structures Decorated with Plasmonic Au Nanoparticles. *ACS Omega* **2019**, *4*, 12071–12080. [CrossRef]
9. Chen, R.; Wang, J.; Xia, Y.; Xiang, L. Near Infrared Light Enhanced Room-Temperature NO_2 Gas Sensing by Hierarchical ZnO Nanorods Functionalized with PbS Quantum Dots. *Sens. Actuators B Chem.* **2018**, *255*, 2538–2545. [CrossRef]
10. Brunelli, D.; Rossi, M. CH_4 Monitoring with Ultra-Low Power Wireless Sensor Network. In *Applications in Electronics Pervading Industry, Environment and Society*; De Gloria, A., Ed.; Springer International Publishing: Cham, Switzerland, 2014; Volume 289, pp. 13–25, ISBN 978-3-319-04369-2.
11. Fàbrega, C.; Casals, O.; Hernández-Ramírez, F.; Prades, J.D. A Review on Efficient Self-Heating in Nanowire Sensors: Prospects for Very-Low Power Devices. *Sens. Actuators B Chem.* **2018**, *256*, 797–811. [CrossRef]
12. Kim, J.-H.; Mirzaei, A.; Kim, H.W.; Kim, S.S. Low Power-Consumption CO Gas Sensors Based on Au-Functionalized SnO_2-ZnO Core-Shell Nanowires. *Sens. Actuators B Chem.* **2018**, *267*, 597–607. [CrossRef]
13. Markiewicz, N.; Casals, O.; Fabrega, C.; Gràcia, I.; Cané, C.; Wasisto, H.S.; Waag, A.; Prades, J.D. Micro Light Plates for Low-Power Photoactivated (Gas) Sensors. *Appl. Phys. Lett.* **2019**, *114*, 053508. [CrossRef]
14. Monereo, O.; Casals, O.; Prades, J.D.; Cirera, A. A Low-Cost Approach to Low-Power Gas Sensors Based on Self-Heating Effects in Large Arrays of Nanostructures. *Procedia Eng.* **2015**, *120*, 787–790. [CrossRef]
15. Prades, J.D.; Jimenez-Diaz, R.; Hernandez-Ramirez, F.; Barth, S.; Cirera, A.; Romano-Rodriguez, A.; Mathur, S.; Morante, J.R. Ultralow Power Consumption Gas Sensors Based on Self-Heated Individual Nanowires. *Appl. Phys. Lett.* **2008**, *93*, 123110. [CrossRef]
16. Qomaruddin; Casals, O.; Šutka, A.; Granz, T.; Waag, A.; Wasisto, H.S.; Prades, J.D.; Fàbrega, C. Visible Light-Driven P-Type Semiconductor Gas Sensors Based on $CaFe_2O_4$ Nanoparticles. *Sensors* **2020**, *20*, 850. [CrossRef]
17. Qomaruddin; Fàbrega, C.; Waag, A.; Šutka, A.; Casals, O.; Wasisto, H.S.; Prades, J.D. Visible Light Activated Room Temperature Gas Sensors Based on $CaFe_2O_4$ Nanopowders. *Proceedings* **2018**, *2*, 834. [CrossRef]

18. Franke, M.E.; Koplin, T.J.; Simon, U. Metal and Metal Oxide Nanoparticles in Chemiresistors: Does the Nanoscale Matter? *Small* **2006**, *2*, 36–50. [CrossRef] [PubMed]
19. Xu, F.; Lv, H.-F.; Wu, S.-Y.; Ho, H.-P. Light-Activated Gas Sensing Activity of ZnO Nanotetrapods Enhanced by Plasmonic Resonant Energy from Au Nanoparticles. *Sens. Actuators B Chem.* **2018**, *259*, 709–716. [CrossRef]
20. Fallah, H.; Asadishad, T.; Shafiei, M.; Shokri, B.; Javadianaghezi, S.; Mohammed, W.S.; Hamidi, S.M. Utilizing ZnO Nanorods for CO Gas Detection by SPR Technique. *Opt. Commun.* **2020**, *463*, 125490. [CrossRef]
21. Kwon, D.-K.; Porte, Y.; Ko, K.Y.; Kim, H.; Myoung, J.-M. High-Performance Flexible ZnO Nanorod UV/Gas Dual Sensors Using Ag Nanoparticle Templates. *ACS Appl. Mater. Interfaces* **2018**, *10*, 31505–31514. [CrossRef]
22. Lupan, O.; Postica, V.; Wolff, N.; Su, J.; Labat, F.; Ciofini, I.; Cavers, H.; Adelung, R.; Polonskyi, O.; Faupel, F.; et al. Low-Temperature Solution Synthesis of Au-Modified ZnO Nanowires for Highly Efficient Hydrogen Nanosensors. *ACS Appl. Mater. Interfaces* **2019**, *11*, 32115–32126. [CrossRef] [PubMed]
23. Huang, T.; Xu, X.-H.N. Synthesis and Characterization of Tunable Rainbow Colored Colloidal Silver Nanoparticles Using Single-Nanoparticle Plasmonic Microscopy and Spectroscopy. *J. Mater. Chem.* **2010**, *20*, 9867. [CrossRef] [PubMed]
24. Wan, Q.; Wang, T.H.; Zhao, J.C. Enhanced Photocatalytic Activity of ZnO Nanotetrapods. *Appl. Phys. Lett.* **2005**, *87*, 083105. [CrossRef]
25. Khan, R.; Yun, J.-H.; Bae, K.-B.; Lee, I.-H. Enhanced Photoluminescence of ZnO Nanorods via Coupling with Localized Surface Plasmon of Au Nanoparticles. *J. Alloys Compd.* **2016**, *682*, 643–646. [CrossRef]
26. Jin, Y.; Wang, J.; Sun, B.; Blakesley, J.C.; Greenham, N.C. Solution-Processed Ultraviolet Photodetectors Based on Colloidal ZnO Nanoparticles. *Nano Lett.* **2008**, *8*, 1649–1653. [CrossRef] [PubMed]
27. Prades, J.D.; Jimenez-Diaz, R.; Manzanares, M.; Hernandez-Ramirez, F.; Cirera, A.; Romano-Rodriguez, A.; Mathur, S.; Morante, J.R. A Model for the Response towards Oxidizing Gases of Photoactivated Sensors Based on Individual SnO_2 Nanowires. *Phys. Chem. Chem. Phys.* **2009**, *11*, 10881–10889. [CrossRef] [PubMed]
28. Bora, T.; Zoepfl, D.; Dutta, J. Importance of Plasmonic Heating on Visible Light Driven Photocatalysis of Gold Nanoparticle Decorated Zinc Oxide Nanorods. *Sci. Rep.* **2016**, *6*, 26913. [CrossRef] [PubMed]
29. Gong, J.; Li, Y.; Deng, Y. UV and Visible Light Controllable Depletion Zone of ZnO-Polyaniline p–n Junction and Its Application in a Photoresponsive Sensor. *Phys. Chem. Chem. Phys.* **2010**, *12*, 14864–14867. [CrossRef]
30. Chen, Y.; Li, X.; Li, X.; Wang, J.; Tang, Z. UV Activated Hollow ZnO Microspheres for Selective Ethanol Sensors at Low Temperatures. *Sens. Actuators B Chem.* **2016**, *232*, 158–164. [CrossRef]
31. Cui, J.; Shi, L.; Xie, T.; Wang, D.; Lin, Y. UV-Light Illumination Room Temperature HCHO Gas-Sensing Mechanism of ZnO with Different Nanostructures. *Sens. Actuators B Chem.* **2016**, *227*, 220–226. [CrossRef]
32. Comini, E.; Faglia, G.; Sberveglieri, G. UV Light Activation of Tin Oxide Thin Films for NO_2 Sensing at Low Temperatures. *Sens. Actuators B Chem.* **2001**, *78*, 73–77. [CrossRef]
33. Chen, C.; Zhang, Q.; Pan, H.; Xie, G.; Su, Y.; Tai, H.; Du, X. Visible Light-Activated Room Temperature NO_2 Sensing with Au-ZnO Nanorod Array Thin Films. In Proceedings of the 2019 IEEE SENSORS, Montreal, QC, Canada, 27–30 October 2019; pp. 1–4.
34. Zhu, Q.; Lu, J.; Wang, Y.; Qin, F.; Shi, Z.; Xu, C. Burstein-Moss Effect Behind Au Surface Plasmon Enhanced Intrinsic Emission of ZnO Microdisks. *Sci. Rep.* **2016**, *6*, 36194. [CrossRef] [PubMed]
35. Chen, S.; Pan, X.; He, H.; Chen, W.; Chen, C.; Dai, W.; Zhang, H.; Ding, P.; Huang, J.; Lu, B.; et al. Enhanced Photoluminescence of Nonpolar P-Type ZnO Film by Surface Plasmon Resonance and Electron Transfer. *Opt. Lett. OL* **2015**, *40*, 649–652. [CrossRef]
36. Korotcenkov, G.; Brinzari, V.; Cho, B.K. Conductometric Gas Sensors Based on Metal Oxides Modified with Gold Nanoparticles: A Review. *Microchim. Acta* **2016**, *183*, 1033–1054. [CrossRef]
37. Chen, C.; Zhang, Q.; Xie, G.; Yao, M.; Pan, H.; Du, H.; Tai, H.; Du, X.; Su, Y. Enhancing Visible Light-Activated NO_2 Sensing Properties of Au NPs Decorated ZnO Nanorods by Localized Surface Plasmon Resonance and Oxygen Vacancies. *Mater. Res. Express* **2020**, *7*, 015924. [CrossRef]
38. Fan, J.; Fábrega, C.; Zamani, R.; Shavel, A.; Güell, F.; Carrete, A.; Andreu, T.; López, A.M.; Morante, J.R.; Arbiol, J.; et al. Solution-Growth and Optoelectronic Properties of ZnO:Cl@ZnS Core–Shell Nanowires with Tunable Shell Thickness. *J. Alloys Compd.* **2013**, *555*, 213–218. [CrossRef]
39. Khan, A.; Jadwisienczak, W.M.; Kordesch, M.E. From Zn Microspheres to Hollow ZnO Microspheres: A Simple Route to the Growth of Large Scale Metallic Zn Microspheres and Hollow ZnO Microspheres. *Phys. E Low-Dimens. Syst. Nanostruct.* **2006**, *33*, 331–335. [CrossRef]
40. Liu, S.; Wang, Z.; Zhang, Y.; Dong, Z.; Zhang, T. Preparation of Zinc Oxide Nanoparticle–Reduced Graphene Oxide–Gold Nanoparticle Hybrids for Detection of NO_2. *RSC Adv.* **2015**, *5*, 91760–91765. [CrossRef]
41. Rai, P.; Kim, Y.-S.; Song, H.-M.; Song, M.-K.; Yu, Y.-T. The Role of Gold Catalyst on the Sensing Behavior of ZnO Nanorods for CO and NO_2 Gases. *Sens. Actuators B Chem.* **2012**, *165*, 133–142. [CrossRef]
42. Wongrat, E.; Chanlek, N.; Chueaiarrom, C.; Samransuksamer, B.; Hongsith, N.; Choopun, S. Low Temperature Ethanol Response Enhancement of ZnO Nanostructures Sensor Decorated with Gold Nanoparticles Exposed to UV Illumination. *Sens. Actuators A Phys.* **2016**, *251*, 188–197. [CrossRef]
43. Barsan, N.; Weimar, U. Conduction Model of Metal Oxide Gas Sensors. *J. Electroceram.* **2001**, *7*, 143–167. [CrossRef]

44. Liao, Z.-M.; Liu, K.-J.; Zhang, J.-M.; Xu, J.; Yu, D.-P. Effect of Surface States on Electron Transport in Individual ZnO Nanowires. *Phys. Lett. A* **2007**, *367*, 207–210. [CrossRef]
45. Barry, T.I.; Stone, F.S.; Tompkins, F.C. The Reactions of Oxygen at Dark and Irradiated Zinc Oxide Surfaces. *Proc. R. Soc. Ser. A. Math. Phys. Eng. Sci.* **1960**, *255*, 124–144. [CrossRef]